

## ORIGINAL RESEARCH

# Intelligent height measurement technology for ground encroachments in large-scale power transmission corridor based on advanced binocular stereovision algorithms

Zhong Tang<sup>1</sup> | Chenglong Jia<sup>1</sup>  | Heng Wang<sup>2</sup> | Shuaiang Rong<sup>3</sup> | Wenbin Zhao<sup>1</sup>

<sup>1</sup>College of Electrical Engineering, Shanghai University of Electrical Power, Shanghai, China

<sup>2</sup>State Grid Henan DC Operation & Maintenance Company, Zhengzhou, China

<sup>3</sup>College of Electrical Engineering, University of Illinois, Illinois, Chicago, USA

## Correspondence

Wenbin Zhao, College of Electrical Engineering, Shanghai University of Electrical Power, Shanghai, 200090, China.

Email: wenbinmax@163.com

## Funding information

National Nature Science Foundation of China, Grant/Award Number: 52177185

## Abstract

To locate the ground encroachments in transmission line corridor effectively, the application of a novel binocular stereo vision (BSV) for distance measurement is realized with improvement and adjustment in calibration and reconstruction process of BSV. Firstly, a calibration method using a 1-D pole with spatial constraints to replace the 2-D calibration object is proposed. The field experiment shows that this method improves the accuracy of the calibration in a large-scale scene by expanding the calibration area. Then, a regulation algorithm to eliminate the difference between focal lengths for binocular cameras is designed to further improve accuracy of calibration. For practical utilization of BSV in the monitor system, the 3-D reconstructions from world coordinate system (WCS) to ground-based system is achieved by rotation and transformation of the reconstructed coordinate system and direct height measurement is realized consequently. Further, based on the calibration method being proposed, the partial calibration with a reduced calibration distribution area is studied considering the probable complex terrain. Height measurement calculations are carried out on both hypothetical and real obstacles to verify the validity of the calibration method and postprocessing algorithms. The results demonstrated that the calibration method algorithms successfully realized the practical application of BSV in large-scale scene with high accuracy. By using this novel BSV technology, the total transmission line inspection cost is expected to be greatly reduced by comparing with manned helicopter and UAV inspections.

## 1 | INTRODUCTION

Electric power plays a vital role in the rapid development of economy. As key components in power transmission system, safety operation of high voltage overhead lines is rather essential. With the rise of power consumption, transmission network grows rapidly in China. In recent years, area expansion of transmission lines greatly contributes to the confliction between the infrastructure and safety of overhead transmission lines. For instance, constructions involving improper operation of cranes often lead to failure of transmission lines, which seriously affect the safety of power grid and even cause casualties. The growth of trees nearby also commonly leads to short circuits of the transmission lines [1]. Due to the rapid growth, transmission lines cover complex terrains, such as lakes, forests, and hills.

This arises more difficulties for transmission line inspection than ever before.

Conventional inspection technologies including foot patrol and helicopter-assisted inspection have become very ineffective for increasing-scale electric network [2, 3]. It is very difficult to clearly determine the precise distance between the ground encroachment and the transmission line by relying on human eyesight from a long distance, which could lead to a high risk of misjudgments in external breakage determinations [4–6]. These traditional inspections are increasingly unable to meet the requirements of the reliable condition monitoring of transmission lines.

The unmanned aerial vehicle (UAV) with Light Detection and Ranging (LiDAR) technique has been widely used as a solution for intelligent and accurate ground encroachment detection of

This is an open access article under the terms of the [Creative Commons Attribution-NonCommercial-NoDerivs](https://creativecommons.org/licenses/by-nc-nd/4.0/) License, which permits use and distribution in any medium, provided the original work is properly cited, the use is non-commercial and no modifications or adaptations are made.

© 2022 The Authors. *IET Generation, Transmission & Distribution* published by John Wiley & Sons Ltd on behalf of The Institution of Engineering and Technology.

transmission line [7, 8]. However, UAV inspection with LiDAR requires costly components such as LiDAR sensors and GPS devices, and needs large computing power for data processing [8]. UAV can also work with digital cameras by using stereovision (SV) technology that can reconstruct the 3-D information of transmission corridor from 2-D binocular images [9, 10]. However, the detection results for UAV with SV technology are usually inaccurate due to dynamic camera coordinates [11]. Another solution for transmission line monitoring is the satellite imaging technology [12]. However, these satellite images generally have lower accuracy due to low image resolutions [13]. As a conclusion, all the above detection methods cannot provide online monitoring with high accuracy and low cost.

In recent years, due to the advantages of low cost and fast responding time, there is a rising interest in applying binocular stereo vision (BSV) for transmission line inspection [14]. This method uses binocular cameras to reconstruct the 3-D coordinates of the object based on parallax [15, 16]. BSV technology has already been successfully used in some typical line monitoring cases, such as ice monitoring for transmission lines [17]. The ice thickness is calculated by 3-D reconstruction, and early warning is generated in the system. In the perspective of application in large-scale scene, for example, for power line inspection, 3-D reconstruction capability of BSV is expected to be utilized for precise distance measurement between plants and lines [14].

Although BSV is suitable for transmission line monitoring for 3-D distance measurement for transmission line monitoring. But this vision-based monitoring method requires complex procedures with sophisticated equipment and is not able to provide constant surveillance. The mobile monitoring devices are not sufficient in manoeuvrability and are at a high cost. In recent years, amounts of cameras were installed on the tower for surveillance, which laid a foundation for BSV, and the monitoring of intrusion in transmission line corridor can be realized theoretically. But improvement and adjustment are required for practical application. BSV generally includes three parts [17]: Firstly, calibration is carried out to build projection model of binocular cameras. Secondly, corresponded points of objects in two images are recognized to obtain disparity. Thirdly, 3-D coordinates of these points are reconstructed based on the model and disparities.

However, practical application of BSV in large-scale scene monitoring is scarcely researched. In this paper, a series of methods and algorithms are proposed to solve the problems in the large-scale overhead line distance measurement experiment. Four problems emerged in the experiment and resolutions are given below. Firstly, the calibration area is too small by using the traditional calibration plane, so the calibration area is enlarged by using the calibration pole method. Secondly, in the calibration process, the difference of focal length of two cameras generated by characteristics of zoom lens leads to an inaccurate calibration process, so the method of adaptive focal length regulation is adopted to reduce the error of calibration results. Thirdly, the coordinate system of reconstruction results is based on the optical axis, which brings great inconvenience to the ground measurement. Therefore, the reconstructed coordinate system is regulated by locating the zero-datum for direct

height measurement of the coordinate system according to the reconstruction results. At last, limitation of the scene terrain results in the calibration array cannot be placed completely, so the calibration is carried out by using part of the calibration pole array, and the relationship between the calibration area and the measurement error is studied, so that the calibration area of the acceptable measurement error range is obtained. The processing results and height measurements are presented on hypothetical and real obstacles to testify the feasibility and effectiveness of the proposed methods and algorithms.

## 2 | FIELD SET-UP FOR BSV IN LARGE-SCALE SCENE BASED ON IMPROVED CALIBRATION METHOD

Conventional 2-D calibration method with checkerboard is mostly used for its flexibility in previous research on the distance measurement of BSV [18, 19]. However, in this section, this method is testified not applicable in large-scale calibration due to the restriction of the calibration area. Therefore, a more flexible calibration method is proposed to broaden the calibration area by applying 1-D calibration pole on positions with space constraints.

### 2.1 | Preliminary reconstruction results of calibration points by using 2-D checkerboard

Mathematic model of BSV is obtained by camera calibration [20]. The conventional Zhang's calibration method [21] is mostly used in camera calibration. A sequence of images of a checkerboard in different angles are utilized in this method, and projection model are calculated with the linear constraint among the corner points in the checkerboard.

The calibration experiment by using 2-D checkerboard was carried out in ultra high voltage (UHV) Engineering Technology (Kunming) National Engineering Laboratory. Image collection equipment are two dome network cameras on the UHV tower. The camera has a DS-2DE4220IW-D type number, with focal length ranging from 4.7 to 94 mm, and supports 16 times digital zoom. Through the PTZ (Pan/Tilt/Zoom) control, it supports 360 horizontally, 90 vertically tilting and position preset function. Two cameras were mounted on a DJ-300 tower about 2 m away from each other and 13 m high from the ground. Images data are captured by computer through WIFI.

Based on Zhang's method, images were then captured of a 3 m × 4 m checkerboard, which is put in front of the tower about 80 m in five different angles. The image of left camera in the first angle is as Figure 1a. In calibration, the checkerboards in five angles are regarded as five calibration planes. Corner points (P1 to P6) between black and white squares in each calibration plane are detected. Figure 1b shows detected points in the first plane. After calibration, stereo parameters are obtained.

Figure 2a shows extrinsic parameters and illustrates the positions of the calibration planes and binocular cameras. Obviously seen, though the position of the calibration plane

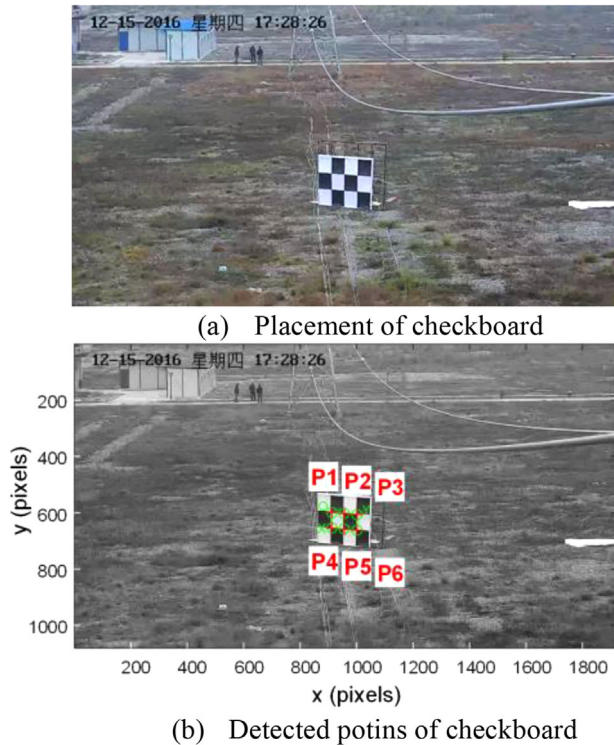


FIGURE 1 Corner points extraction

is approximately calculated, the positions of the cameras are not left and right as in reality, indicating that the conventional calibration method is not applicable in the large-scale scene.

To further prove this, the reconstruction of the corner points in Figure 1b is calculated, as shown in Figure 2b and the coordinates of P1 to P6 are displayed in Table 1. The distances between P1 to P2, P2 to P3, P3 to P6, P1 to P4, P4 to P5, and P5 to P6 on the plane are 1 m. But the results of the distances showed a great average error, that is 16.58 m. These flawed results indicate that checkerboard cannot achieve a qualified calibration.

What's more, the checkerboard takes a lot of efforts to manufacture and use. During the field set-up, the checkerboard is 3 m × 4 m, making it quite hard to hold stable for the stationary image capture process against the wind outdoor, and it is very difficult to make a non-deformed checkerboard in this scale and to put in different angles. In addition, with a massive workload in the transportation, it still counts a small proportion in the view as shown in Figure 1a. In general, the 2-D checkerboard method is proved inefficient and not applicable for the calibration in large-scale scene. Thus, a new calibration method using a 1-D pole instead of a checkerboard is addressed to expand horizons of calibration.

## 2.2 | Improved reconstruction results by using 1D calibration pole with space constraints

The field set-up is the same. But the preset positions of the cameras and the focal lengths are regulated because the calibration

area increases. The parameters of the left and right cameras are set to (P357: T00), Z003; (P358: T02), Z003, respectively, where P/T/Z are the abbreviations of Pan/Tilt/Zoom, which represents the horizontal angle, vertical angle, and times of zoom of the camera. The units for P and T are both degrees in the angular system. Then a pole ruler is stretched to 4 m length and marked with a white attachment each of 1 m to replace the checkerboard for calibration, as in Figure 3a. Then it is put in the due front of the tower 75 m, and every 5 m horizontally and vertically from the first site and five sets in each direction. Then the images of the pole were captured in all 25 positions. But makers are considered corner points and are extracted by using control point selection tool (cpselect) in MATLAB software. By selecting control points in two binocular images simultaneously, the location information of the corner points in image coordinate system (ICS) is extracted and would be converted into that in world coordinate system (WCS) automatically. To maximize the utilization of extracted points, all the data are divided into six calibration planes as is shown in Figure 3b. Each plane consists of four poles and each pole concludes four points. Positions are numbered as  $P_{11}$  to  $P_{64}$ , and  $P_{00}$  is regarded as a reference position during locating the pole.

Experiment set-up is as in Figure 3c. The reconstructed coordinate system is based on the left camera coordinate system. In Figure 3, calibration points form a 3 m × 20 m × 20 m cube so that the calibration space is greatly extended compared with a 3 m × 4 m checkerboard in the WCS.

In the camera coordinate system, the calibration area is also greatly increased with the improved calibration method being applied. Based on the homography matrix in extrinsic parameters of binocular cameras, the overlapping field of view (FOV) are obtained consequently [22]. All the five calibration planes of the calibration method with the checkerboard, six calibration planes of the calibration method with the pole and the FOV line are shown in Figure 4. After the calculation, the ratio of calibration area to the overlapping FOV in the conventional method is 0.88% and in the improved method the ratio is 27.72%.

After calibration, Figure 5a shows that the positions of cameras and six calibration planes are closer to reality compared with those in Figure 2a. Figure 5b illustrates the reconstruction of the calibration points. And the height measurement in Table 2 showed a great improvement compared with the reconstruction results in Table 1. The average error decreased from 16.58 to 0.12 m, indicating that the reconstruction results are greatly improved with the improved calibration method.

It yet can be seen that the position of right camera is more forward than the left camera, and the positions of the planes are not parallel from the optic axis of the cameras. This indicates that the intrinsic and extrinsic parameters need further optimization.

The reconstruction result showed that the improved calibration method is proved to be applicable in the large-scale scene for transmission line monitoring. But it cannot meet the requirement of practical application in complex terrain and need further regulation for high accuracy.

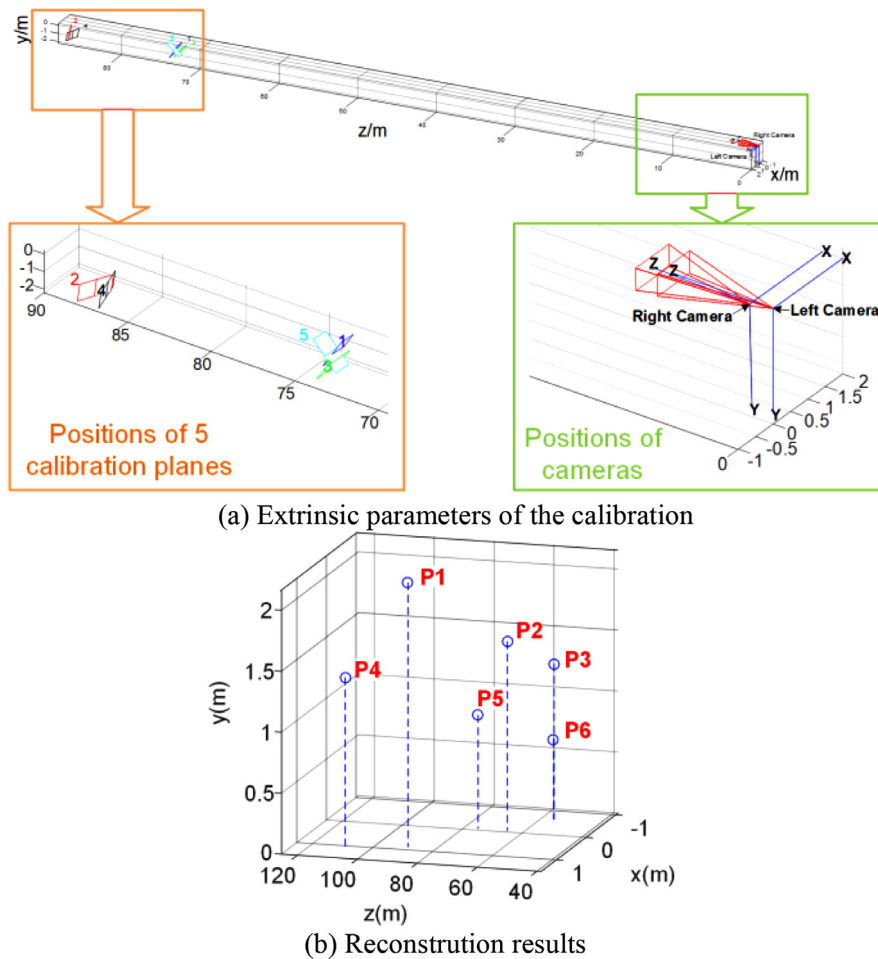


**FIGURE 2** Calibration and reconstruction results with the checkerboard

**TABLE 1** Reconstruction results

Coordinates/m	P1	P2	P3	P4	P5	P6
X	0.8778	-0.0659	-0.6508	1.0925	-0.0717	-0.6576
Y	2.1666	1.5478	1.2744	1.3972	0.9276	0.6505
Z	89.4278	65.5818	55.7176	108.2160	75.3489	56.0124
Reconstructed distances/m						
P1-P2	P2-P3	P3-P6	P1-P4	P4-P5	P5-P6	Average error/m
23.8727	9.8854	0.6901	18.8052	32.8911	19.3474	16.58
Real distance/m						
P1-P2	P2-P3	P3-P6	P1-P4	P4-P5	P5-P6	
2	2	3	3	2	2	

### 3 | POST-PROCESSING OF RECONSTRUCTION RESULTS FOR PRACTICAL APPLICATIONS

For practical purposes, the accuracy is increased first and simplification of the calculation is realized. Generating errors

of the calibration results of parameters is inevitable due to the experiment set-up [23]. Hence, an algorithm is designed to reduce this effect by eliminating the difference between the focal lengths of two cameras. Further, to simplify the calibration method proposed and the reconstruction results, an algorithm to transform the reconstruction results from WCS to



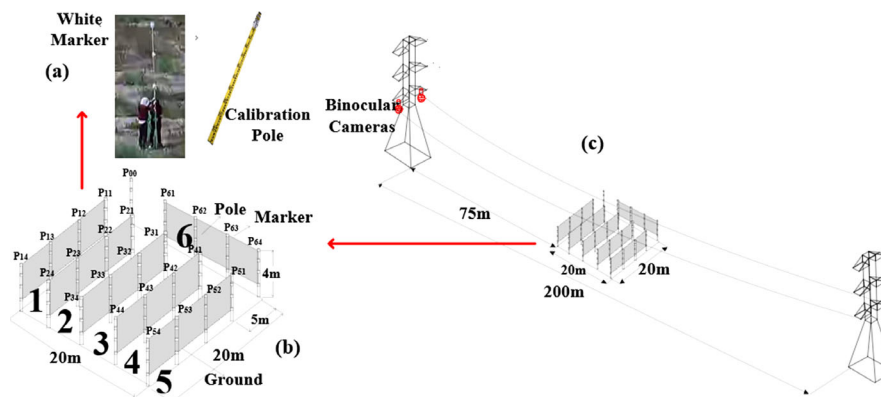


FIGURE 3 Set-up of the pole for calibration

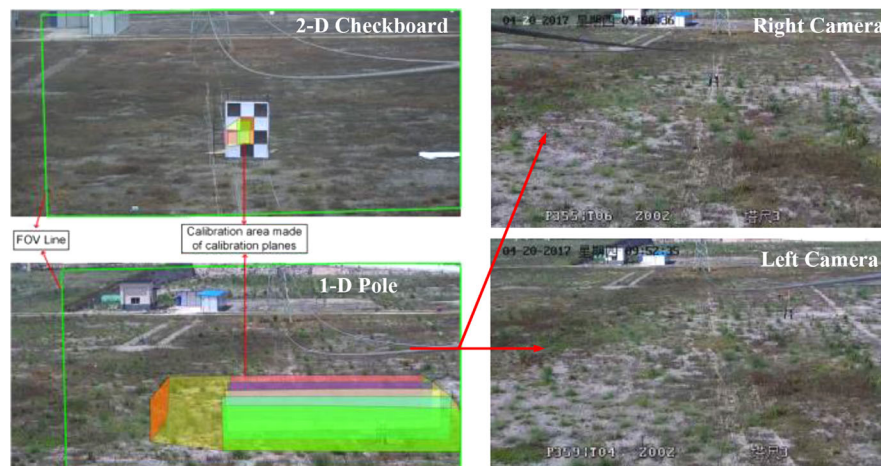
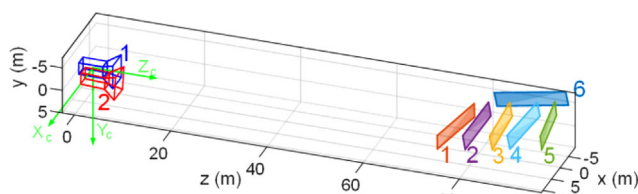
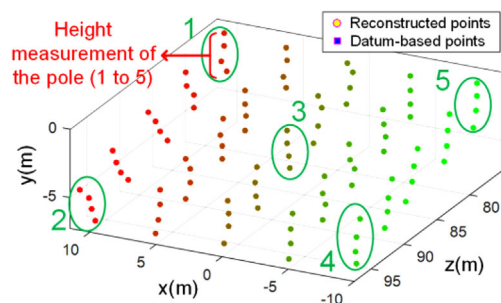


FIGURE 4 Comparison of calibration area between two calibration methods



(a) Extrinsic Parameters of the calibration with the pole



(b) Reconstruction results compared with datum-based coordinates of points

FIGURE 5 Calibration and reconstruction results with the improved method

TABLE 2 Height measurement of the pole in five positions

Measured height/m (ideal height: 3 m)					
1	2	3	4	5	Average error/m
3.5731	3.0711	2.9596	3.0572	2.9448	0.1212

ground-based coordinate system (GCS) is proposed, and partial calibration for application in complex terrains is studied.

### 3.1 | Regulation of focal lengths

In previous studies of accuracy analysis for BSV, the focal lengths of binocular cameras are commonly assumed equivalent [24] for prime lens. But difference of focal lengths between two surveillance cameras is unneglectable in large-scale BSV system. To further improve the accuracy of calibration, an algorithm to regulate the focal lengths is put forward.

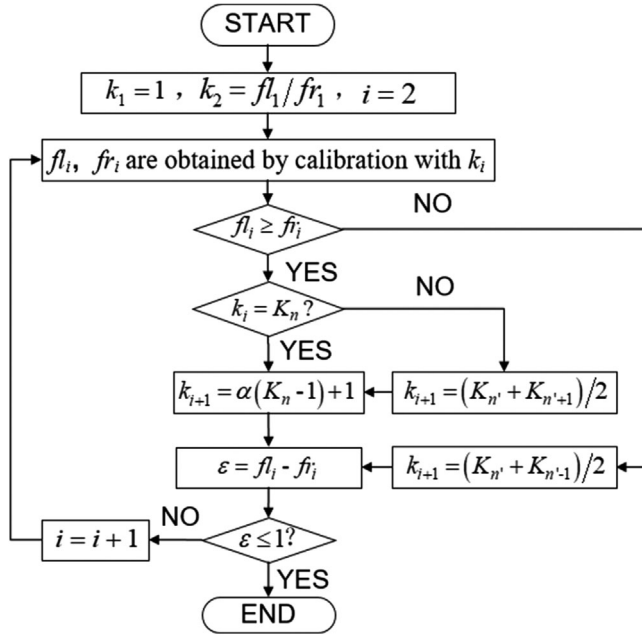


FIGURE 6 Flowchart of focal length regulation algorithm

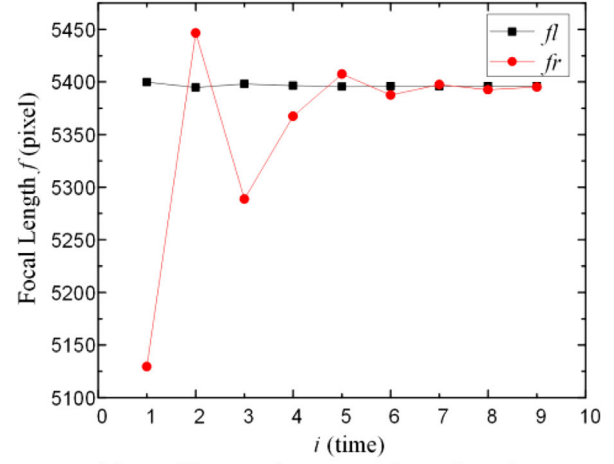
Figure 5a highlights that position of cameras differs in the Z direction, indicating that the focal lengths of two cameras vary. Of all intrinsic parameters in surveillance cameras, only the focal length is set manually; others are determined by inner structure characteristic of cameras and not adjustable. The difference between focal lengths of two cameras is caused by low mechanical precision and artificial error during the focal length setting. This situation could lead to errors of calibration based on the ideal stereo vision model [21].

Changes of focal length directly reflect on the image size in digital zooming. Image size grows as digital camera zooms in, vice versa. Therefore, the difference between focal lengths can be eliminated by resizing the corresponding image. The proposed regulation method for focus length optimization is shown in Figure 6. It is noted that the image resizing method adopted here is Nearest-Neighbour Interpolation for image size reduction and Linear Interpolation for image size increment.

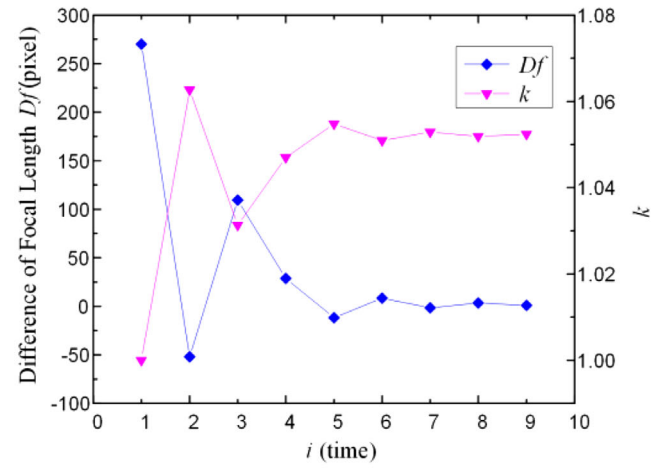
In the first calibration, the focal lengths of the left and right cameras are  $f_{l1} = 5184.2$ ,  $f_{r1} = 5088.2$ , respectively, and the unit is pixel. Set a proportional factor  $k_i$  ( $k_i \geq 1$ ) to apply in the  $i$  time of calibration to regulate the points from the right image and  $k_1$  is set to 1. Considering that the calibrated left camera focal length  $f_{l1}$  is larger than the right camera focal length  $f_{r1}$ , when  $i = 2$ , the initial value of proportional factor is obtained by (1).

$$k_2 = f_{l1}/f_{r1}. \quad (1)$$

$f_{li}$  and  $f_{ri}$  are calculated by calibration with the right coordinate points regulated by  $k_i$ . After the  $i$  time of calibration,  $\{k_1, \dots, k_i\}$



(a) Changes in camera focus lengths



(b) Differences in Focus length and k value

FIGURE 7 Results of focal length regulation

is sorted from small to large as  $\{K_1, \dots, K_n\}$  to calculate  $k_{i+1}$  under the following situations:

1. When  $f_{li} > f_{ri}$  and  $k_i = K_n$ ,  $k_{i+1}$  is obtained with an amplifying coefficient  $\alpha$ .

$$k_{i+1} = \alpha(k_n - 1) + 1. \quad (2)$$

2. When  $f_{li} > f_{ri}$  and  $k_i = K_n$ ,  $k_{i+1}$  should be between  $K_{n'}$  and  $K_{n'+1}$ , and  $n'$  represents the place of  $k_i$  in  $\{K_1, \dots, K_n\}$ .

$$k_{i+1} = (k_{n'} + k_{n'+1})/2. \quad (3)$$

3. When  $f_{li} < f_{ri}$ ,  $k_i$  should be declined with (4).

$$k_{i+1} = (k_{n'} + k_{n'-1})/2. \quad (4)$$

The difference  $\varepsilon$  is obtained by

$$\varepsilon = f_{li} - f_{ri}. \quad (5)$$



FIGURE 8 Extraction of the end points and obscured bottom points

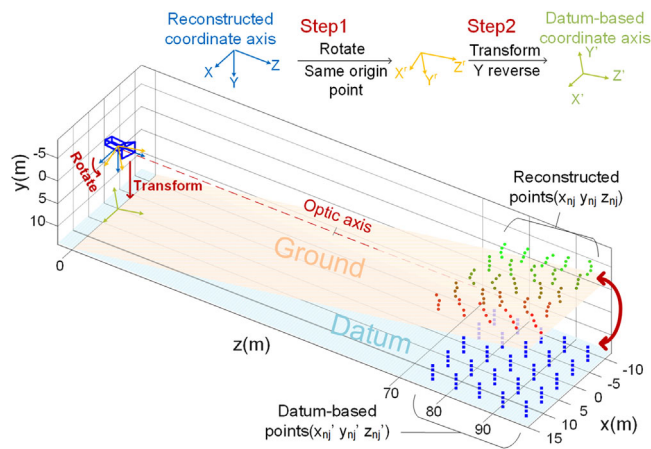


FIGURE 9 Rotation and transformation in zero datum location

In the proportional scaling method,  $\alpha$  is set to 1.5, and when  $\varepsilon < 1$ , the process is stopped. The reasons for the value settings of  $\alpha$  and  $\varepsilon$  are explained as following.

In order to get a precise focus length regulation result, the difference between the pixel values of the right and left camera images should be as close as to 0, that is, the ideal value of  $\varepsilon$  should be 0. However, since the proportional scaling method is applied in adjusting the right image size, in addition with the manufacturing capability of the camera image unit, it is impossible to get  $\varepsilon$  equal to 0 both mathematically and physically. For the simplification of compactional calculation,  $\varepsilon$  is set to 1 in this paper.

For the focus length regulation process, it is noted that the proportional scaling is applied on the right image. In the case of right image pixel size is smaller than that of the left image, that is,  $k_i$  is larger than 1; we should increase the value of  $k_{i+1}$  so that the size of the right image can get larger and get closer to that of the left image. According to Equation (2),  $\alpha$  should be at least larger than 1 to make  $k_{i+1}$  larger than  $k_i$ . Since the initial ratio of  $f_i$  and  $f_l$  is generally within 1.2, to get a fast coverage of the calculation,  $\alpha$  is set to 1.5 as the optimized value.

The results of  $f_l$ ,  $f_r$  during regulation are in Figure 7. Figure 7a illustrates that  $f_r$  shows a fluctuation around  $f_l$  and ends up approximate with  $f_l$ .  $f_l$  has a slight variation because the optimization of calibration process is based on the maximum likelihood estimation method [19] and involves both calibration points of the left and the right. The left and right focal lengths are respectively 5390 and 5395.1. In Figure 7b, the difference gradually converges and declines to 0.9 with change of  $k$  after nine times of calibration. The results showed that the algorithm efficiently eliminates the difference between calibrated focal lengths of two cameras, indicating that the projection model is optimized by decreasing difference of intrinsic parameters in binocular cameras.

### 3.2 | WCS to GCS transformation of advanced BSV

Practically, the environment of the worksite can be rather complex. The bottom of objects covered by plants on the ground makes the height measurement impossible, because two end points of the object need to be extracted as in Figure 8. Therefore, a method to transform the reconstructed coordinate system from WCS to GCS based on the ground of the tower is proposed to realize direct height measurement. Trees and vehicles are the main threat objects. Therefore the main concern in transmission line monitoring is the height.

The reconstructed GCS is based on the left camera coordinate and the  $Z$  direction of the coordinate system is the optical axis, which is not parallel from the ground. Quasi Newton method [25] is used to rotate the coordinate system in three directions to obtain the GCS. Figure 9 shows the reconstructed points in WCS and the real point coordinates measured in GCS. The reference points for the transformation are the horizontal datum, that is, virtual ground in the GCS. By calculating angles between coordinates of reconstructed points and ideal datum-based points in three directions, the reconstructed WCS is rotated and the ground in GCS is regulated to be parallel to the  $X$ - $Y$  plane. Then by reversing  $Y$  axis and transformation of





FIGURE 10 Work site with complex environment and places for the pole

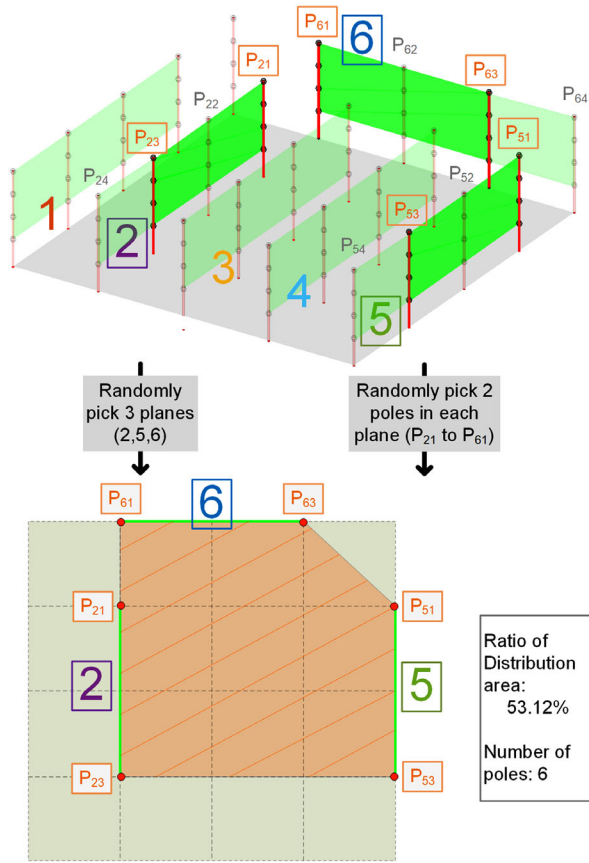


FIGURE 11 Radom process in partial calibration

origin point for 13 m, which is the height of the cameras from the ground, the zero datum of reconstructed coordinate system is obtained.

Rotation of reconstructed calibration points is shown in (6).

$$\begin{bmatrix} x'_{nj} & y'_{nj} & z'_{nj} & 1 \end{bmatrix}^T = \begin{bmatrix} x_{nj} & y_{nj} & z_{nj} & 1 \end{bmatrix}^T R_1 R_2 R_3. \quad (6)$$

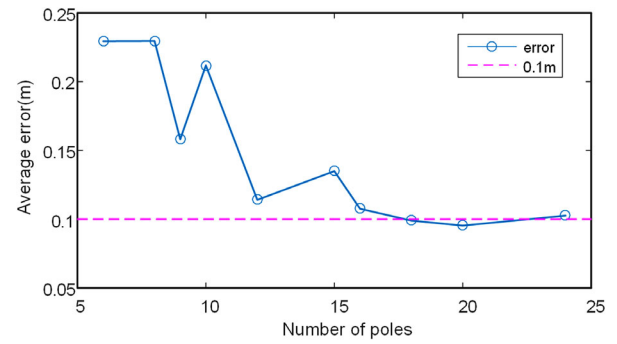


FIGURE 12 Relationship between average error of human height measurement and the number of poles used in the partial calibration

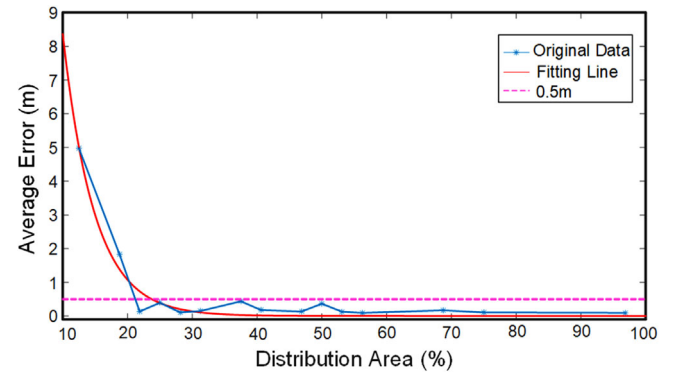


FIGURE 13 Relationship between average error of human height measurement and the distribution area of poles used in the partial calibration

$[x_{nj} \ y_{nj} \ z_{nj} \ 1]^T$  are homogeneous coordinates of  $j$ th points from top on the  $n$ th pole,  $[x'_{nj} \ y'_{nj} \ z'_{nj} \ 1]^T$  are homogeneous coordinates after rotation.  $R_1, R_2, R_3$  are matrix of rotation constructed by angles of rotation in  $X, Y, Z$  directions. Then the geometric mean error of four calibration points on the  $n$ th pole is obtained in (7).



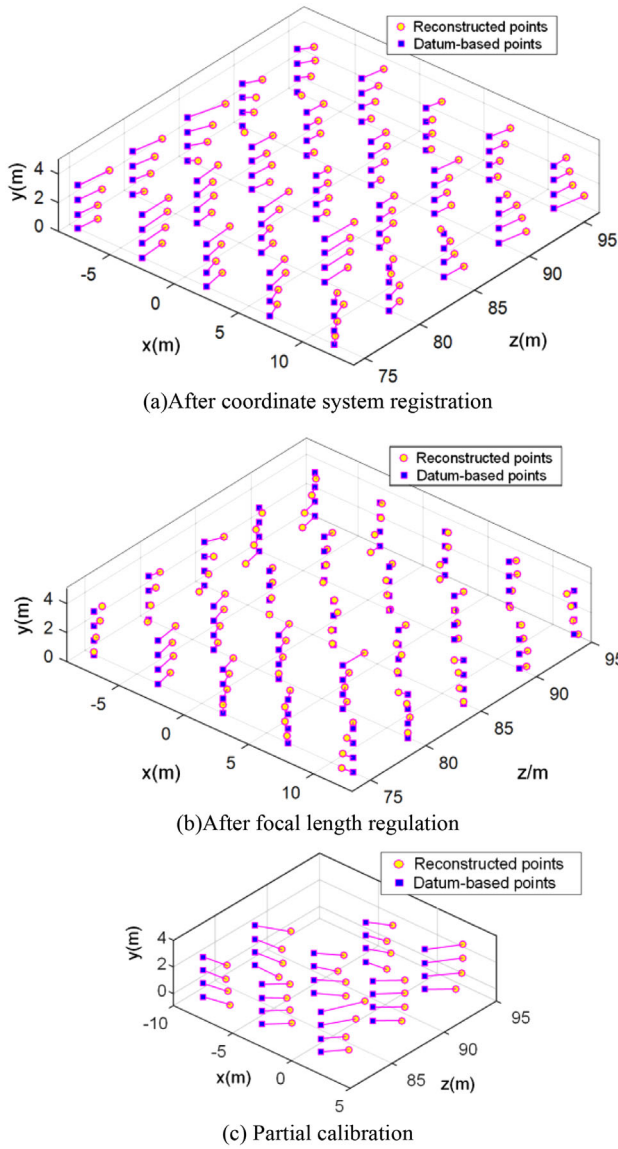


FIGURE 14 Reconstruction results

$$H_n = \frac{1}{2} \sqrt{\sum_{j=1}^4 (x_{nj}^r - x_{nj}')^2 + (y_{nj}^r - y_{nj}')^2 + (z_{nj}^r - z_{nj}')^2}. \quad (7)$$

$(x_{nj}', y_{nj}', z_{nj}')$  is the correspondent ideal GCS. The largest geometric mean error of four points in all 25 poles is taken as the objective function as in (8).

$$H = \max(H_n), \text{ where } n = 1, \dots, 25. \quad (8)$$

With the subjective function and its first-order derivative, searching direction of the optimal solution is constructed by the quasi-Newton method and angles of rotation are obtained.

Therefore, by calculating the datum of the reconstructed coordinate system, only the highest point of the object needs

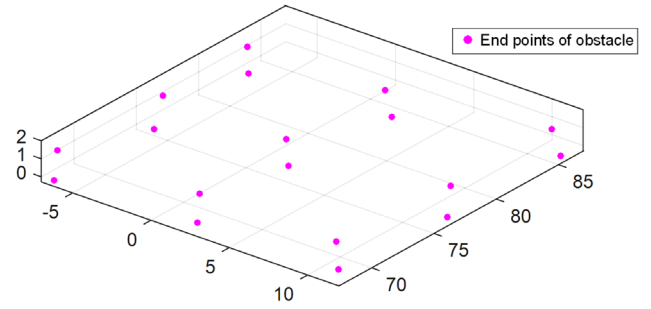


FIGURE 15 Reconstruction of the end points of the obstacle in nine positions

TABLE 3 Height measurement results

Method	Two-point			One-point	
	Before $f$ regulation	After $f$ regulation	Partial calibration	GCS	Partial calibration
Position number					
1	1.512 2	1.535 6	1.964 9	1.783 3	1.951 4
2	1.766 5	1.780 7	1.605 1	1.545 5	2.053 4
3	1.451 9	1.520 7	1.799 0	1.598 5	2.335 0
4	1.385 6	1.475 5	1.390 6	1.820 7	2.142 0
5	1.437 0	1.564 7	1.499 2	1.705 7	2.187 0
6	1.468 0	1.648 3	1.590 9	1.716 0	2.338 5
7	1.401 8	1.578 9	1.701 4	2.016 0	1.858 6
8	1.413 9	1.587 2	2.135 7	1.876 7	1.756 0
9	1.491 8	1.760 3	1.705 5	1.604 6	1.725 3
$ME(\%)$	13.90	6.64	0.57	10.46	18.52
$SE(m)$	0.26	0.15	0.22	0.21	0.39

$ME$  and  $SE$  are respectively the mean relative error and the standard error of the nine height measurements. The real height of the hypothetical obstacle is 1.72 m.

to be identified and reconstructed in GCS, and the height can be obtained with the coordinates of one point.

### 3.3 | Partial calibration in complex environment

The calibration with a pole greatly improved accuracy of camera calibration. But it has disadvantages especially when situations on the ground under the conductors are complex and positions of poles are restricted, as in Figure 10. Reducing the number and the distribution area of poles for calibration is vital in this situation. Therefore, the reconstruction errors are analyzed with various numbers and distribution area of poles.

To build the projection model of binocular cameras, at least two poles in three calibration planes are required [18]. There are a total of four poles in six planes in the experiment. For reducing pole distribution area, two to four poles in three to six planes are randomly extracted 10 times respectively for calibration to obtain 120 groups of stereo parameters, which are all used to reconstruct the obstacle height in nine positions in the images



**FIGURE 16** Binocular camera setup on a real 220-kV tower

**TABLE 4** Parameters of the camera and the local processor

Device	Parameter	Value
Camera	Model	DS-2DE4220IW-D/W
	Focus length	4.7–94 mm, 20 × Zoom
	Maximum power	18 W
Image processor	Memory	62 G
	Processor	Intel Xeon@2.30 GHz
	GPU	Nvidia RTX 2080 Ti
	Operation system	Ubuntu 16.04 LTS

for evaluation. One example of the random process is shown in Figure 11.

In the samples, some calibration results may lead to large errors because of some singular solutions. Hence, the 10% largest errors of each pole number are eliminated. The relationship of pole number and the average error of the data is shown in Figure 12. The whole trend of the average error decreased with the increasing pole number, but it does not show a clear mathematic relationship. That's because there are two factors in the same number of poles affecting the results, that is, the number of poles in each calibration plane and number of planes.

Therefore, the distribution area is regarded as an indicator for calibration accuracy. Average errors of various distribution areas are computed as shown in Figure 13, and the 10% largest errors are removed equally. The whole distribution area is 400 m<sup>2</sup> obtained by polygon area formed with all 25 poles. Errors of obstacle height measurement are calculated by all calibration parameters, and statistical results are made according to the ratio of polygon area formed by randomly chosen poles to the whole area. The statistical results are shown in Figure 13.

When the distribution area reached 22%, average error dropped to 0.14 m and remains less than 0.5 m within a small range. The relationship of calculation error and ratio of distribution area is assumed as an exponential function. After curve fitting, (9) is obtained with 95% confidence bounds and is a guidance to ratio of poles distribution in partial calibration for

**TABLE 5** Reconstruction results of real obstacles

Testing object	Coordinates of blue circle/m	Coordinates of red circle/m	Distance measurement/m
Vegetation	(6.65, 9.62, 4.25)	(3.56, 5.37, 22.46)	12.9
Balloon	(5.51, 4.01, 22.14)	(5.21, 3.09, 26.61)	4.5
Crane	(6.67, 3.61, 21.53)	(0.39, 8.37, 37.52)	17.8

complex terrain.

$$E = 65.08e^{-0.2051x}, \quad (9)$$

where  $x$  is the ratio of distribution area of chosen poles to the whole area,  $E$  is the calculated average error of obstacle height.

## 4 | DISCUSSIONS OF THE EFFICIENCY OF USING PARTIAL CALIBRATION IN PRACTICAL APPLICATIONS

To testify the validity of the calibration method, the reconstruction errors of calibration points and height measurement results are calculated for the regulations of focal length and WCS. Measurement results of partial calibration parameters are included.

### 4.1 | Error analysis of reconstruction for calibration points

Twenty-five groups of fixed calibration points for complete calibration and eight groups for partial calibration are reconstructed. The reconstruction results after the registration of the coordinate system, after the regulation of focal lengths, and after applying partial calibration, compared with the real position coordinates, are shown in Figures 14a, 14b, and 14c, respectively.

Compared with Figure 9, the reconstructed points are generally regulated to the position of the datum-based points. The error  $H$  in function (8) before focal length regulation is 3.0395, and it is 0.2668 after regulation the error of measurement is reduced by focal length regulation. The error  $H$  for partial calibration is 4.1326, indicating that the partial calibration is not accurate as complete calibration despite of the advantage of less area.

### 4.2 | Height measurement results of hypothetical obstacle

To verify the feasibility of the coordinate measuring system, a height measurement of a hypothetical obstacle in nine positions is carried out. The height of the obstacle without occlusion was measured. The reconstruction results are showed in Figure 15.

Table 3 highlights that the height measurement results and errors calculated with distance measurement between two end

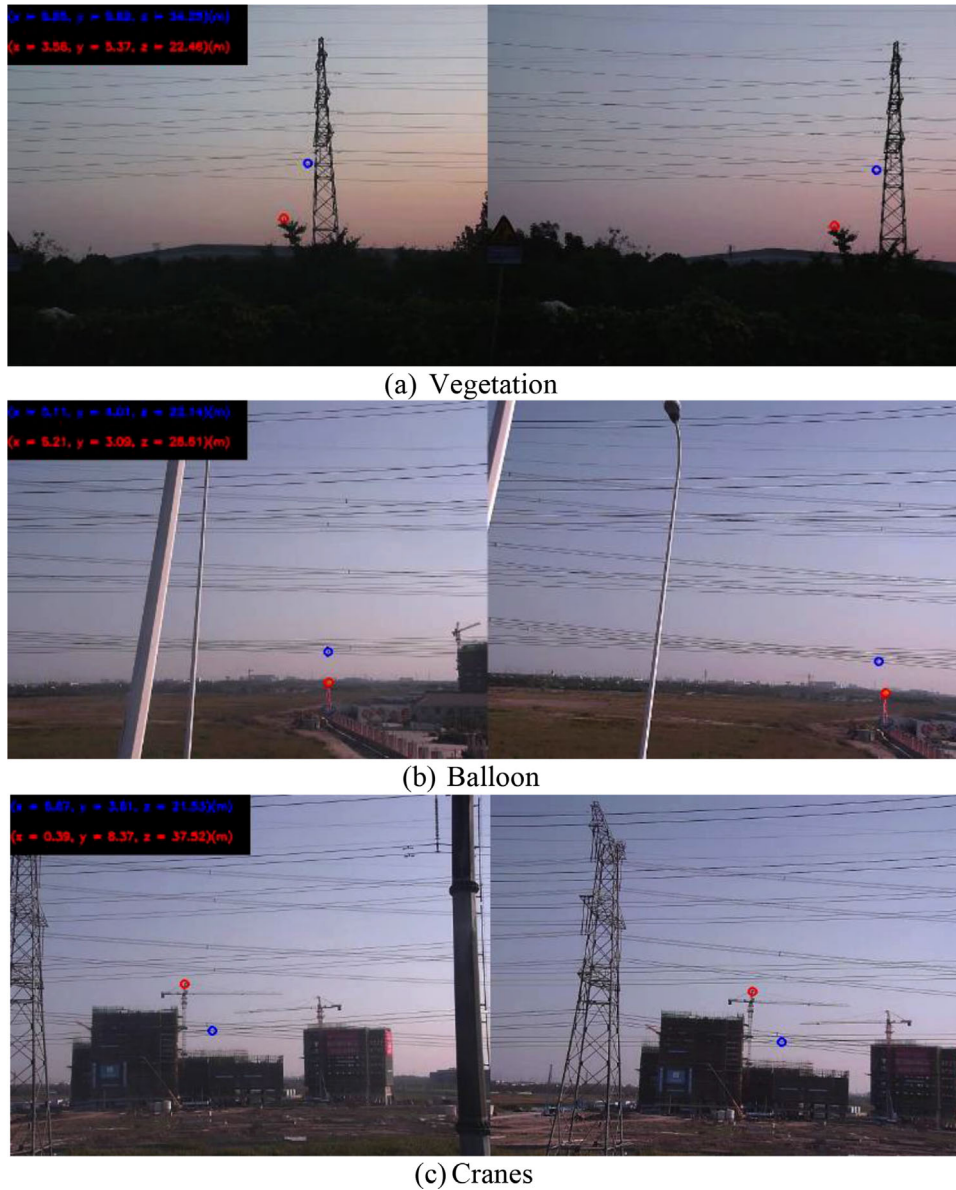


**FIGURE 17** Binocular camera measurements of different types of obstacles

points and the Y coordinate of one top point of the obstacle under different procedures. The real height of the obstacle is 1.72 m. In the row 1, 2, and 4, it is showed that the mean error and the standard error both reduce, from 13.9% to 6.64% and 0.26 to 0.15m with the two-point method and the focal length regulation. Then, after the coordinate system is regulated, the obstacle height is calculated by the single point method. The mean relative error is 10.46%, higher than that of the two-point method, but still less than that before the focal length regulation. And the standard error shares the same trend. This result indicates that the focal length regulation improves the accuracy and stability of distance measurement effectively and the calculation of height is simplified in a tolerable range of error.

As for the results with the partial calibration in row 3 and 5, mean relative error with two points method is 0.57%, which is

lowest of all. But with one point method, it is 18.52%, higher than all. And the standard error is respectively 0.22 and 0.39. This suggested that the partial calibration performs well in 22% of the visual field but not very stable in the datum-based coordinate system with one point. However, the results in row 5 are generally larger than 1.72m, which indicate that the datum locating progress may need improvement in partial calibration.

### 4.3 | Height measurement results of real obstacles

For the precise assessment of the state of the ground encroachments in transmission channels, it is necessary to propose a practical test of the BSV technology on real obstacles such



as cranes and vegetations. The BSV method should be able to accurately identify the location and height of the encroachments. Therefore, binocular cameras were mounted on a real 220 kV power tower, as shown in Figure 16. Wireless communication is applied in the image data collection and transferring between the tower and local image processor. The detailed parameters of the camera and the processor hardware are listed in Table 4. The recognition results for three typical obstacles including crane, vegetation and balloon are shown in Figure 17.

The red circle in Figure 17 indicates the location of the highest point of the encroachments, and the blue circle represents the location of the nearest transmission line with the red circle, and their three-dimensional coordinates are shown in the upper left corner of the image. According to the coordinates of the location of the blue circle and the coordinates of the location of the red circle, the distance between the target and the transmission line can be calculated, and the distance measurement results are shown in Table 5. It is noted that the real heights of the vegetation and the crane are 9.9 and 21.8 m, respectively, which means the measuring errors of the BSV technology is less than 0.3 m for the large transmission corridor scene.

#### 4.4 | Cost-effectiveness and viability of proposed technology

Compared with the traditional manned helicopter inspection, the proposed BSV technology only need 20 cameras per km in case the power tower spacing is approximately 100 m in average. The total line inspection costs would be greatly reduced, since only surveillance camera purchase and basic maintenances are required. Compared with the UAV inspection, the biggest advantages of this BSV method is that it can do the constant surveillance.

For the practical application of the novel binocular calibration method proposed in this paper, it is noted that the calibration results would be obviously influenced by the visible-light image qualities of the binocular cameras. For example, uneven illumination problems could make calibration failures. In order to increase the reliability and viability of this proposed technology, image pre-processing algorithms such as de-fogging, anti-shanking, and de-noising should be applied on the initial camera images before calibration.

## 5 | CONCLUSION

A new calibration method and a sequent of algorithms for calibration and reconstruction of stereo vision in large scale overhead transmission lines are proposed to realize application of stereo vision in large scales (approximate 100 m distance) of high accuracy. Two methods are introduced to simplify the computation progress in industrial application by locating the datum and conducting partial calibration.

With comparison of the innovative calibration method using a pole and with a checkerboard, the new method enables the application of BSV in transmission line corridor and increase

the ratio of calibration area to the FOV from 0.88% to 27.72%. The regulation algorithm of focal length decreases the difference between focal lengths of binocular cameras, relative error of measurement for obstacle height reduces from 13.9% to 6.64%. The practical application is also realized with a guaranteed accuracy. Direct height measurement after the reconstructed coordinate regulation showed that the relative error of measurement with one-point method is 10.46%, which is 0.17 m as absolute error. For complex environment of transmission lines, relationship of measurement error and the distribution area of poles are further studied. And it is derived that when ratio of distribution area reaches 22% of the whole area, mean error maintain in less than 0.1 m.

In the future work, the automatic recognition of the feature points will be further researched and more experiments for partial calibration will be conducted to testify the robustness of this method.

#### AUTHOR CONTRIBUTIONS

Zhong Tang: Conceptualization, Methodology; Cheng long Jia: Software, Writing – original draft; Shuaiang Rong: Writing – review & editing, Software; Heng Wang: Investigation; Wen bin Zhao: Validation

#### ACKNOWLEDGEMENT

This work was supported by National Nature Science Foundation of China (52177185). Experimental set-up and experimental data collection in this paper are supported by the staff of the National Engineering Laboratory of the UHV Engineering Technology (Kunming). In addition, the experimental equipment in this article is provided by the limited public power technology of Shanghai Xun Rui. The authors would like to express great appreciation for their help.

#### CONFLICT OF INTEREST

All co-authors have no conflicts of interest to disclose.

#### DATA AVAILABILITY STATEMENT

Data sharing not applicable to this article as no datasets were generated or analysed during the current study.

#### ORCID

Chenglong Jia  <https://orcid.org/0000-0002-8734-4513>

#### REFERENCES

1. Gugel, H. et al.: Vegetation-related outages on transmission lines in north America. In: Proceedings of IEEE Power and Energy Society General Meeting, Portland, OR, pp. 1–5 (2018)
2. Aggarwal, R.K., Johns, A.T., Jayasinghe, J.A.S.B., Su, W.: An overview of the condition monitoring of overhead lines. *J. Electr. Pow. Syst. Res.* 53(1), 15–22 (2000)
3. Future inspection of overhead transmission lines. Electric Power Research Institute, Palo Alto, CA, U.S. Rep. 1016921 (2008)
4. Yang, L., Fan, J., Liu, Y., Li, E., Peng, J., Liang, Z.: A review on state-of-the-art power line inspection techniques. *IEEE Trans. Instrum. Meas.* 69(12), 9350–9365 (2020)
5. Xu, C., Li, Q., Zhou, Q., Zhang, S., Yu, D., Ma, Y.: Power line-guided automatic electric transmission line inspection system. *IEEE Trans. Instrum. Meas.* 71, 1–18 (2022)



6. Sikorska-Lukasiewicz, K.: Methods of automatic vegetation encroachment detection for high voltage power lines. In: *Proceedings of SPIE Radioelectronics System Conference*, Jachranka, Poland, Feb. (2020)
7. Foudeh, H.A., Luk, P.C.-K., Whidborne, J.F.: An advanced unmanned aerial vehicle (UAV) approach via learning-based control for overhead power line monitoring: A comprehensive review. *IEEE Access* 9, 130410–130433 (2021)
8. Wu, Y. et al.: Overhead transmission line parameter reconstruction for UAV inspection based on tunneling magnetoresistive sensors and inverse models. *IEEE Trans. Power Del.* 34(3), 819–827 (2019)
9. Han, Y. et al.: Study on unmanned aerial vehicle with neural network stereovision perception for reducing pesticide and water saving in precision agriculture. In: *2021 3rd International Academic Exchange Conference on Science and Technology Innovation (IAECST)*, pp. 651–654 (2021)
10. Sahu, S., Karmakar, A., Hari, P.: 3D pose estimation of UAVs using Stereovision. In: *2019 International Conference on Range Technology (ICORT)* (2019)
11. Babineca, A., Apeltauerb, J.: On accuracy of position estimation from aerial imagery captured by low-flying UAVs. *Int. J. Trans. Sci. Tech.* 5(3), 152–166 (2016)
12. Qayyum, A. et al.: Monitoring of vegetation near power lines based on dynamic programming using satellite stereo images. In: *Proceedings of the IEEE International Conference on Smart Instrumentation Measurement and Applications*, pp. 1–6 (2014)
13. Future inspection of overhead transmission lines. *Electric Power Res. Inst.* Palo Alto, CA, U.S. Rep. 1016921 (2008)
14. Rong, S., He, L., Du, L., Li, Z., Yu, S.: Intelligent detection of vegetation encroachment of power lines with advanced stereovision. *IEEE Trans. Power Del.* 36(6), 3477–3485 (2021)
15. Tang, Y., Zhu, M., Chen, Z., Wu, C., Chen, B., Li, C., Li, L.: Seismic performance evaluation of recycled aggregate concrete-filled steel tubular columns with field strain detected via a novel mark-free vision method. *Structures* 37, 426–441 (2022)
16. Tang, Y., Li, L., Wang, C., Chen, M., Feng, W., Zou, X., Huang, K.: Real-time detection of surface deformation and strain in recycled aggregate concrete-filled steel tubular columns via four-ocular vision. *Rob. Comput. Integr. Manuf.* 59, 36–46 (2019)
17. Huang, X., Zhang, F., Li, H., Liu, X.: An online technology for measuring icing shape on conductor based on vision and force sensors. *IEEE J. IEEE Trans. Instrum. Meas.* 66(12), 3180–3189 (2017)
18. Sun, J., Wang, P., Qin, Z., Qiao, H.: Overview of camera calibration for computer vision. In: *WCICA*, Shenyang, China, pp. 86–92 (2014)
19. Vilaça, J.L., Fonseca, J.C., Pinho, A.M.: Calibration procedure for 3D measurement systems using two cameras and a laser line. *Elsevier J. Opt. Laser Technol.* 41(2), 112–119 (2009)
20. Tsai, R.Y.: An efficient and accurate camera calibration technique for 3D machine vision. In: *Proceedings of the IEEE Conference on Computer Vision & Pattern Recognition*, pp. 364–374 (1986)
21. Zhang, Z.: A flexible new technique for camera calibration. *IEEE Trans. Pattern Anal. Mach. Intell.* 22(11), 1330–1334 (2000)
22. Khan, S., Shah, M.: Consistent labeling of tracked objects in multiple cameras with overlapping fields of view. *IEEE Trans. Pattern Anal. Mach. Intell.* 25(10), 1355–1360 (2003)
23. Yang, L., Wang, B., Zhang, R., Zhou, H., Wang, R.: Analysis on location accuracy for binocular stereo vision system. *IEEE Photon. J.* 10(1) (2017)
24. Aguilar, J.J., Torres, F., Lope, M.A.: Stereo vision for 3D measurement: Accuracy analysis, calibration and industrial applications. *Elsevier J. Meas.* 18(4), 193–200 (1996)
25. Davidon, W.C.: Variable metric method for minimization. *J. Siam J. Optimiz.* 1(1), 1–17 (1991)

**How to cite this article:** Tang, Z., Jia, C., Wang, H., Rong, S., Zhao, W.: Intelligent height measurement technology for ground encroachments in large-scale power transmission corridor based on advanced binocular stereovision algorithms. *IET Gener. Transm. Distrib.* 17, 448–460 (2023).  
<https://doi.org/10.1049/gtd2.12688>